Microfluidic Platform for Automatic Quantification of Malaria Parasite Invasion Under Physiological Flow Conditions

Emma Kals[a,b,1], Morten Kals[b], Viola Introini[a,b], Boyko Vodenicharski[b], Jurij Kotar[b], Julian C. Rayner[a,1], and Pietro Cicuta[b,1]

[a]Cambridge Institute for Medical Research, University of Cambridge, Cambridge, UK
[b]Cavendish Laboratory, University of Cambridge, Cambridge, UK
[1]Corresponding author

July 29, 2025

Abstract

Understanding the impact of forces generated by blood flow on biological processes in the circulatory system, such as the growth of malaria parasites, is currently limited by the lack of experimental systems that integrate them. Recent systematic quantification of the growth of *Plasmodium falciparum* - the species that causes the majority of malaria mortality - under a range of shaking conditions has shown that parasite invasion of erythrocytes is affected by the shear stress to which the interacting cells are exposed. Blood flow could similarly impact shear stress and therefore invasion *in vivo*, but there is currently no method to precisely test the impact of flow-induced forces on parasite invasion. We have developed a microfluidic device with four channels, each with dimensions similar to those of a post-capillary venule, but with different flow velocities. Highly synchronised *P. falciparum* parasites are injected into the device, and parasite egress and invasion are quantified using newly developed custom video analysis, which fully automates cell type identification and trajectory tracking. The device was tested with both wild-type *P. falciparum* lines and lines where genes encoding proteins involved in parasite attachment had been deleted. Deletion of Erythrocyte Binding Antigen 175 (PfEBA175) has a significant impact on invasion under flow, but not in static culture. These findings establish for the first time that flow conditions may have a critical effect on parasite invasion. The method can be applied to other biological processes affected by fluid motion, such as cell adhesion, migration, and mechanotransduction.

1 Introduction

Malaria is a devastating disease responsible for over 600,000 deaths annually, with the majority of deaths caused by *Plasmodium falciparum* infections [1]. The blood stage of the parasite's life cycle, which is responsible for all the clinical symptoms of the disease, involves parasites developing and multiplying inside erythrocytes, eventually forming a schizont that egresses, releasing individual parasites known as merozoites. Once merozoites are released, there is typically a time window of less than a minute before they find, attach to and invade a new host erythrocyte [2]. Parasites in newly infected erythrocytes are initially in a form termed the ring stage that then develop over the subsequent 48 hrs into multinucleated schizonts [3, 4].

P. falciparum invasion of and development within human erythrocytes occur in a variety of niches throughout the body. A key site of invasion is thought to be the microvasculature, as postmortem analysis has shown a high level of attachment of infected erythrocytes to capillaries and postcapillary venules in organs in patients with severe malaria [5]. More recent investigations have also provided evidence that other key sites of invasion are the bone marrow [6] and the spleen [7, 8]. In all these environments, fluid flow is present, generating shear forces that could impact the invasion and subsequent development of parasites.

Most parasite growth and invasion assays poorly represent the *in vivo* tissue environment of invasion, as they are carried out in static *in vitro* conditions with blood sedimented to the bottom of tissue culture flasks or plates. The need for new assays was highlighted by our recent results, which showed that fluid motion generated by orbital shaking can both increase and decrease invasion rates. At shear forces comparable to those measured previously in the microvasculature, growth was reduced across wild-type lines, with the magnitude of the effect greater in lines missing key proteins known to be involved in early steps of erythrocyte attachment [9]. Orbital shakers, however, generate variable flow conditions across the well and hence non-uniform shear stress fields [10]. This motivated us to develop an assay that would better mimic the fluid motion typical of blood vessels and thus the resultant forces.

Many microfluidic devices have been developed to mimic the conditions of the circulatory system, as reviewed by [11]. Microfluidic devices have also been built to explore other aspects of malaria biology, such as infected erythrocyte deformability [12, 13, 14], sorting of infected erythrocytes from non-infected [15, 16] and investigating the cytoadhesion of infected erythrocytes to endothelial proteins or cells [17, 18, 19]. However, no microfluidic devices have been developed to specifically follow malaria invasion under flow conditions.

The microfluidic setup presented here allows invasion of *P. falciparum* into human erythrocytes to be tracked under controlled flow conditions. Although parasite invasion could in principle occur under a very wide range of flow conditions, postcapillary vessels are likely a common site for invasion because schizonts sequester there before they rupture and release invasive merozoites [5]. Post-capillary vessels have dimensions of roughly 10-$40\,\mu\mathrm{m}$ and flow velocities of 0.2-$2\,\mathrm{mm/s}$; the venules that follow have dimensions of 0.1-$20\,\mathrm{mm}$ and flow velocities of 2-$8\,\mathrm{mm\,s}$, based on human measurements in the conjunctival pre-capillary arterioles of the eye [20, 21] and in human fingers [22]. In our device, we achieve flow velocities ranging from $0.02\,\mu\mathrm{m\,s^{-1}}$-$0.45\,\mu\mathrm{m\,s^{-1}}$ in four parallel channels, each with a different flow rate. The highest flow rate tested results in a wall shear stress (WSS) of $0.4\,\mathrm{N\,m^{-2}}$. We tightly synchronise our *P. falciparum* parasites before loading the device so that most circulating schizonts egress within a few minutes, resulting in a high rate of invasion as the sample flows through the channels. We also developed an image analysis pipeline that enables the automated identification and tracking of different cell types, allowing us to quantify the invasion rate.

This device has allowed direct measurements of how flow affects invasion. There was no measurable difference in the invasion rate with increasing flow rates for the wild-type lines NF54 and 3D7, but increasing flow velocity did significantly reduce invasion of a parasite line in which the invasion ligand PfEBA175 had been deleted. Our results thus suggest that certain parasite ligands may play a more crucial role during invasion in the bloodstream under flow conditions. The device we have developed has the potential to be applied to other parasite and blood cell studies.

2 Results

2.1 Design of parallel-flow microfluidic device for erythrocyte invasion assay

We developed a PDMS microfluidic device with four parallel channels, where each can be driven with a different flow rate ranging from $20\,\mu\mathrm{m\,s^{-1}}$-$450\,\mu\mathrm{m\,s^{-1}}$. Invasion is observed using video microscopy, and invasion rates are quantified through automated image analysis; the design is illustrated in Fig. 1. The chip has two inlets, one for loading and one for driving the flow from a piezoelectric disc pump. The pump maintains a constant pressure at the inlet using a feedback controller, which is set to a pressure range of 190-240 mBar. The inlet then branches into four parallel channels with identical dimensions. Each channel is $6.7\,\mu\mathrm{m}$ high and $27.7\,\mathrm{cm}$ long. To allow a high rate of egress and invasion in the sample observation over at least a $10\,\mathrm{min}$ time window is required, which limits the maximum flow velocity to be $460\,\mu\mathrm{m\,s^{-1}}$. The channel depth of $6.7\,\mu\mathrm{m}$ ensures that there is a single layer of erythrocytes, which is necessary to allow automated detection of erythrocytes in brightfield. Channels deeper than $6.7\,\mu\mathrm{m}$ were tested but resulted in out-of-focus erythrocytes and multiple layers of erythrocytes, which hindered automated cell tracking, Fig. S1. Each channel has an outlet connected to a vertical water column of varying heights, which generates different backpressures and results in a distinct flow velocity, allowing four different velocities to be compared simultaneously in the same chip run. There are valves on the water column which are set to block the water column when loading, ensuring rapid loading for all channels. The valves are then switched after loading to connect the water columns. The channels are $100\,\mu\mathrm{m}$ wide, meaning that all four channels fit into a single field of view with the 20x objective. Observations are made at a single point close to the outlet.

2.2 Tight synchronisation of *Plasmodium falciparum* parasites ensures a high invasion rate in flow

To facilitate a high invasion rate within a short window of time, the parasites were highly synchronised through multiple developmental cycles (see Methods), then treated with 'Compound 2' for 3-5.5 hours. Compound 2 is a *P. falciparum* Protein Kinase G inhibitor which blocks schizont egress, resulting in the accumulation of highly mature schizonts pre-egress [23]. Once Compound 2 is removed, the parasites will egress approximately 15 minutes later. As the washing steps, transferring to the microscope, and loading take around 10 minutes, the schizonts typically start egressing within 5 minutes of the channels being loaded. This protocol ensures that the majority of parasites are at the same very late schizont stage when loaded into the device and will start egressing quickly once loaded. This maximises the number of invasion events observed during each experimental run, and allows a well-defined timeline in the analysis.

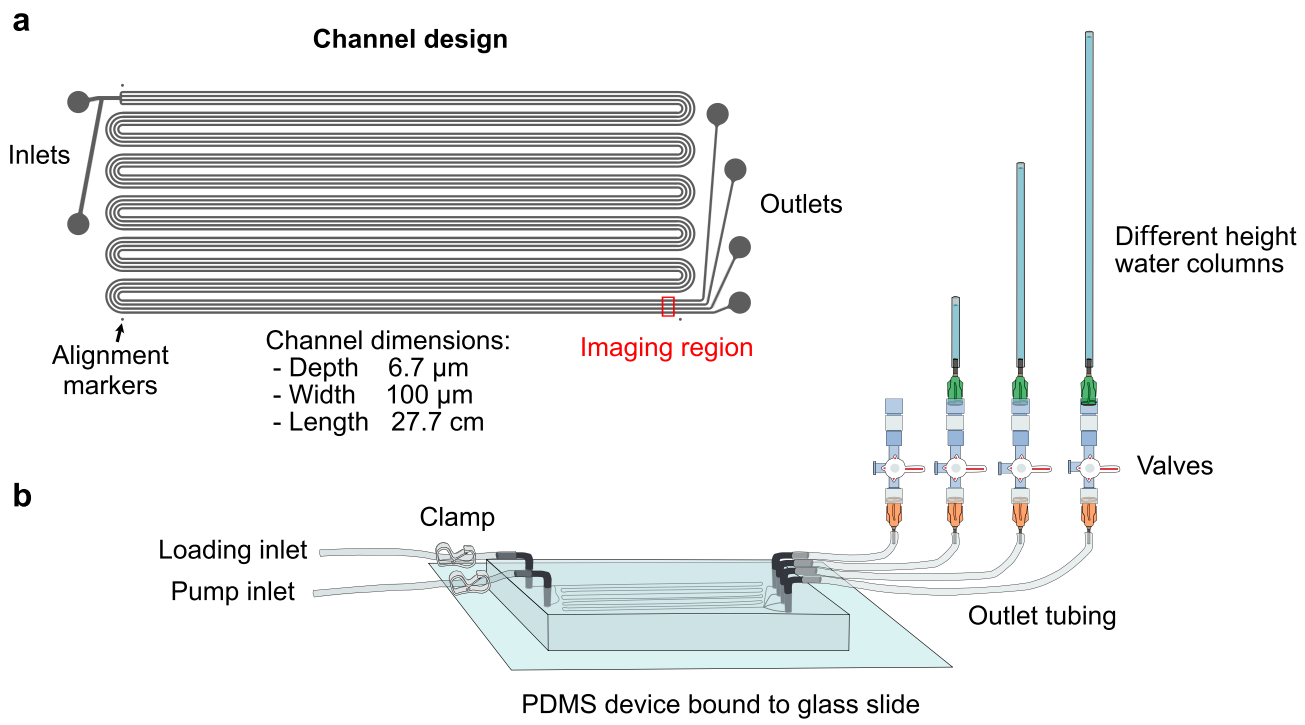

Figure 1: **A PDMS chip has been designed to enable parallel measurements of cells flowing in four different wall shear profiles. (a)** Shows the 2D channel design, which is printed onto photoresist on a silicon wafer with a height of $6.7\,\mu\mathrm{m}$. This is then cast in PDMS to create the chip. **(b)** Shows how the tubing is attached to the PDMS devices. One inlet allows loading, and the other is connected to a pressure pump that drives the flow. There are clamps on the inlet tubing to control which is connected to the device. The inlet channel branches into four channels that snake back and forth, each with its own outlet. Each outlet is connected to a water column of different heights that generates backpressure, with the result that each channel has a different flow velocity. There are valves on the water columns that can block the channels and allow rapid homogeneous loading of all the channels.

2.3 Automated cell identification and tracking

The channels are imaged at a single imaging field of view close to the outlet, as shown in 1a. The sample is initially homogenous throughout the device; therefore, the cell counts in the first few minutes, before egress, will be the same in all channels. The sample then begins to egress, and invade, as it flows through the device, as shown in 2a. The flow rate determines how long it takes for cells that would have been in the inlet at the start of the experiment to reach the imaging field of view. That time interval is the longest that we include in our analysis, thus ensuring that all the invasions measured will have occurred in the channel under the measured steady flow rate.

In order to quantify invasion, we have automated the process of cell type identification and velocity tracking. Videos of the channels are recorded in both brightfield and fluorescence. Automated detection was configured to identify erythrocytes, schizonts, merozoites, rings, and cell debris. The cells are tracked as they pass through the $224\,\mu\mathrm{m}$ of the imaging region. Erythrocytes were detected using brightfield images based on cell size and shape, while parasite stages were stained with the DNA dye Sybr Green, which labels parasite nuclei but not erythrocytes, as they are anucleate. Schizonts were distinguished from rings and merozoites by their large, bright fluorescent signal, reflecting the multiple parasites, and therefore multiple copies of genomic DNA (gDNA) they contain. In contrast, rings and merozoites each contain a single copy of gDNA and therefore exhibit weaker, dimmer fluorescence. Examples of the different cell types are shown in Fig. S2. In order to distinguish rings (parasites that have invaded a new erythrocyte) from free merozoites that happen to visually overlap with an erythrocyte as they are both carried along by flow, we scored rings only where an erythrocyte has a weak fluorescent signal that travels with it across the entire imaging window. Sometimes when schizonts rupture, in addition to free merozoites, a clump of merozoites or other membrane debris is released. We therefore quantified an additional category, called 'cell debris' (fluorescent material of intermediate intensity), to ensure that we did not count these clumped parasites, which are unlikely to successfully invade, as either schizonts or merozoites.

With this experimental design, we expect to see: (1) an almost constant population of erythrocytes, since the number

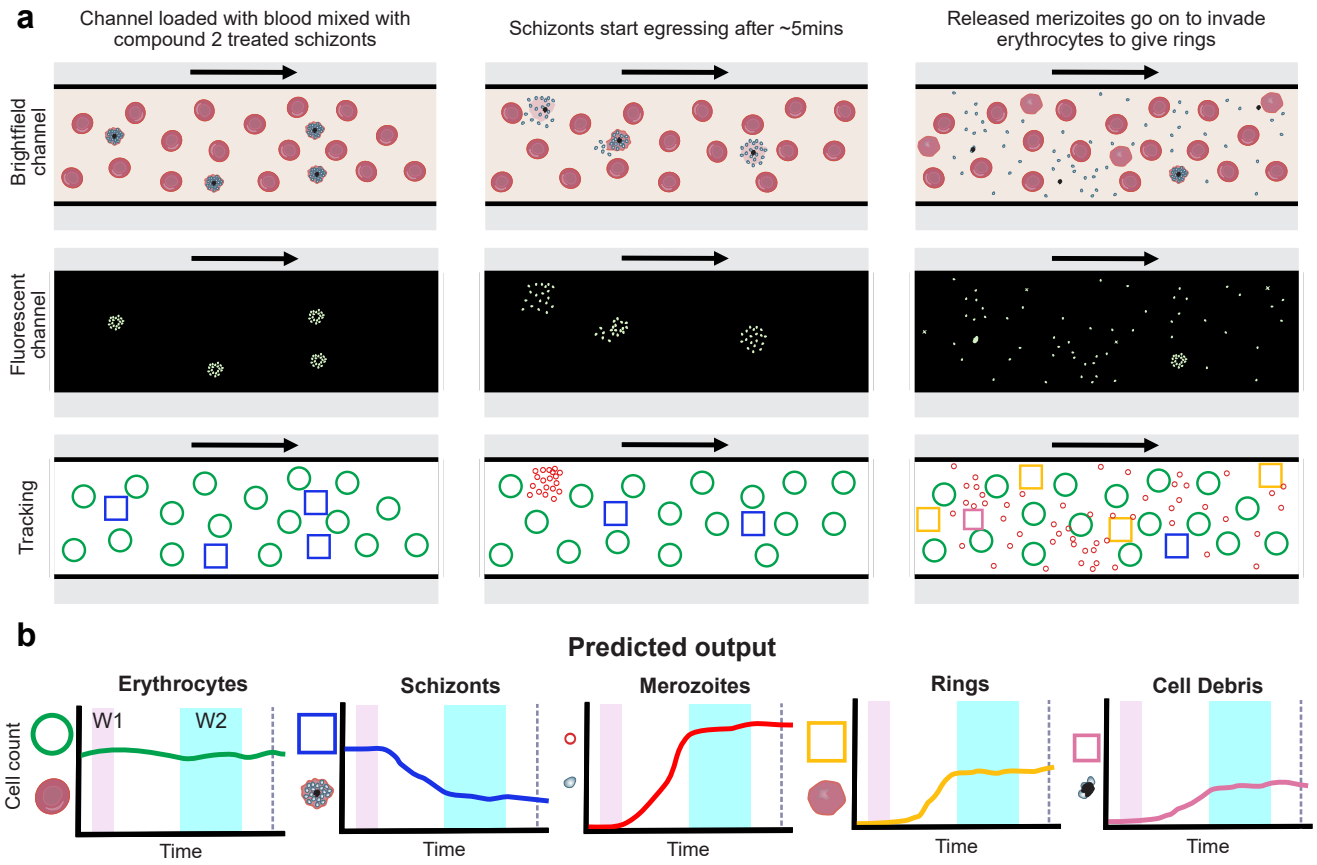

Figure 2: **Experiment design (a)** Cartoon to show how the different cell types are identified throughout the experiment in our imaging window, which is close to the outlet. The experiment starts when the sample is injected into the channel. To begin with, throughout the channel, only erythrocytes (green circles) and schizonts (blue squares) are present. Then, after ∼5 mins, the schizonts start to egress throughout the channel, releasing the merozoites (red circles). By the end of the video, some of the released merozoites have invaded erythrocytes and formed rings (yellow squares). **(b)** Trends of the predicted changes in the four different cell types, and cell debris. Invasion rates are determined by looking at the change in cell count between time window 1 (W1), highlighted in pink shading, and time window 2 (W2) in blue shading. A vertical line represents the time point at which cells that started at the inlet port at time zero pass through the imaging field of view, the position of which is determined by integrating the flow velocity of the cells in each channel. No data is used after this time point, as any invasion that occurs after this line could have occurred before the cells entered the microfluidic channel.

of infected erythrocytes in any parasite culture is low relative to the overall number of erythrocytes (usually <5 %). However, given the tight synchrony of the starting parasites, we should expect a (2) drop in the population of schizonts 5-10 mins after injection into the devices, as they mature and rupture after Compound 2 has been removed, and then (3) a subsequent increase in the number of free merozoites (from a near zero starting population) as they are released from the egressing schizonts. Finally, (4) as the released merozoites invade erythrocytes, the population of rings should increase slightly later than when merozoites first appear, as outlined in Fig. 2b.

2.4 Automated tracking was able to identify different cell types with a high accuracy rate

We carried out at least four biological replicates (each performed with samples prepared on different days and blood from different donors) for each of two wild-type *Plasmodium falciparum* lines (NF54 and 3D7). We first visually confirmed that egress had occurred and that released merozoites invade erythrocytes to produce rings, Fig. S6. We then assessed tracking accuracy by manually annotating cell types in selected frames and comparing them to the automated analysis, which demonstrated a high level of accuracy. Table 1 shows the overall accuracy based on manually labelled images from four experiments and three time points (1, 5 and 8 minutes after invasion). For each sample frame, the number of

Table 1: Average error rates comparing manual and automated counts at a given time point. Time points after 1, 5 and 8 minutes of invasion. The error rates were calculated by comparing frames in which the different cell types were manually counted to the counts for the same frames that were determined using the automated analysis code.

Parameter	Erythrocytes	Schizonts	Merozoites	Rings	Cell debris
Error rate	16%	34%	4%	14%	51%
Total counted	2322	57	247	150	15

erythrocytes, merozoites, rings, schizonts and cell debris present in each channel was manually counted. This was then compared to the mean cell counts per channel reported by the automated analysis at the timestamp of that frame. The error rate is calculated as the difference between the manual and automated cell counts divided by the manual cell count. If both counts are zero, the error is set to zero. If the manual count for a cell type was zero, the error for that repeat was excluded from the average. See Table S1 for the full list of error rates.

Next, we explored how the population of each cell type changed over time for each channel. An example is shown in Fig. 3, with similar plots for the remaining experiments in Fig. S7. Broadly, the populations changed as expected (Fig. 2b), with an initial reduction in schizonts followed by an increase in meozoites and rings, confirming that the automated cell tracking method was detecting the sequential biological steps of schizont rupture, merozoite egress and invasion. Tracking the average speed of all erythrocytes across channels confirmed that the back-pressure approach resulted in different flow velocities, Fig. S8. Repeat 2 of NF54 for example has flow velocities ranging from $35\,\mu\mathrm{m\,s^{-1}}$ in channel 1 to $320\,\mu\mathrm{m\,s^{-1}}$ in channel 4. Fig. S8 confirms that the flow velocities of the different cell types are also highly consistent, indicating that the size or other properties of the cells do not generally affect their speed. There are some notable exceptions, where cells, most often merozoites, become adhered to the glass coverlip for either very short or longer durations, resulting in a temporary drop in the recorded speed for that species.

2.5 Invasion efficiency was quantified by calculating the proportion of rings

The invasion rate can be calculated by measuring the relative change in the proportion of rings between two time windows: an early window 1 (W1) which provides the cell count just after loading and before schizonts begin to egress, and a later window 2 (W2), provides the cell count after the bulk of successful invasion events have occurred. The default settings for W1 were between 0.5 and 3 mins after the start of the experiment, and W2 was between 8 and 15 mins. Window 1 is started after at least 30 seconds to allow the system to stabilise, and the flow velocities to settle after the experiment is started. The end of W1 and the beginning of W2 were chosen based on observations of the video files and cell count traces over time, and the selection of points where the transition from pre-egress to post-invasion occurred. The timing of egress is fairly consistent, as it is determined by the time since Compound 2 was removed. The end of W2 was set to $15\,\mathrm{min}$ as default, but was adjusted on a channel by channel basis to a) consider the flow velocity to ensure only parasites that were in the device at the beginning of the experiment are included, b) not include any significant changes in haematocrit and c) last for longer if the flow velocity is very low and the cell counts are stable to improve statistical accuracy. By adjusting the time window based on the flow velocity and channel length, we ensure that only egress and invasion that occur under flow in the channel are considered, and not events that occurred in the inlet before they are exposed to flow conditions.

The change in cell count for each cell type can then be calculated by subtracting the mean count in window 2 C_{W2} from the mean count in window 1 C_{W1}, namely $\Delta\mathrm{C} = \mathrm{C}_{W2} - \mathrm{C}_{W1}$. For example, we compute the proportion of rings as:

$$\text{Proportion rings} = \frac{\Delta\text{Rings}}{\Delta\text{Rings} + \Delta\text{Merozoites}} \tag{1}$$

Proportion of rings was the main metric we used to measure the invasion rate; it effectively captures the number of egressed merozoites that have successfully invaded erythrocytes. For all experiments we also calculated invasion per schizont as Invasions per schizont $= -\Delta\text{Rings}/\Delta\text{Schizonts}$, but we found this metric had a low signal to noise ratio due to the small number of schizonts present in each experiment (often less than one visible in the field of view at any point in time, as opposed to tens of rings and merozoites in window 2).

2.6 Invasion efficiency for 3D7 and NF54 shows no significant difference under flow

We began by assessing the invasion of wild-type lines NF54 and 3D7 under different flow velocities. The NF54 strain is most likely of West African origin [24], and 3D7 is a clone of NF54 [24] that has been cultured independently for 30 years and, while being genetically very similar [25], has multiple diverged phenotypes [26, 27, 28]. As each run resulted

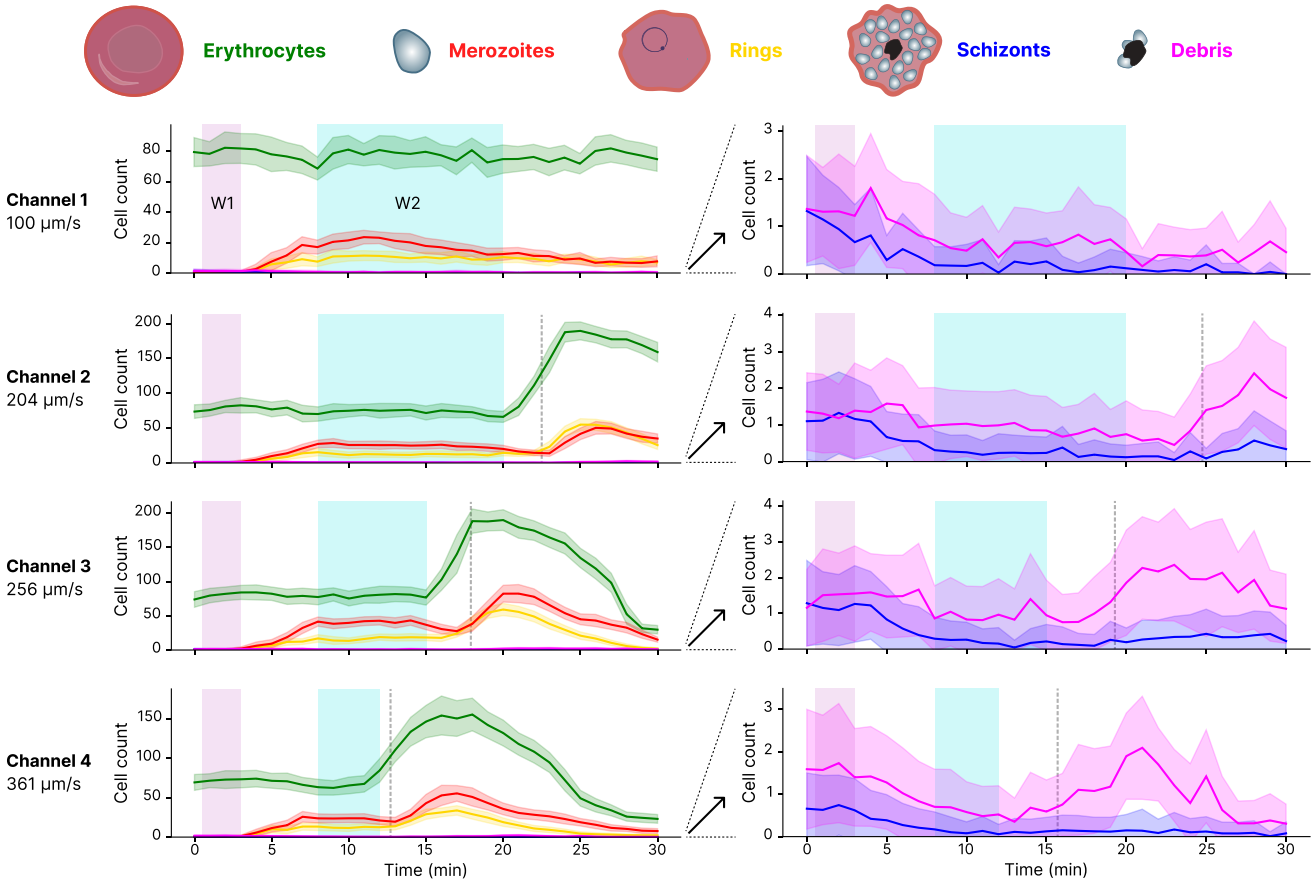

Figure 3: **Example from a single experiment of tracking the populations of cells in each of the four channels.** The data shown is for a single experiment run with the wild-type line NF54. Cell count refers to the number of cells we count in our field of view for a given channel at a given point in time, averaged over a $30\,\mathrm{s}$ interval. This averages all the cells that are tracked as they flow through the imaging window in the $30\,\mathrm{s}$ window. The graphs on the right show the same data as on the left but for a smaller cell count range, to visualise what happens with the schizont and cell debris populations where there are many fewer individual cells. The different colours show the different cell types: green is erythrocytes, red is merozoites, yellow is rings, blue is schizonts, and pink is debris. The time windows are highlighted with window 1 (W1) highlighted in pink shading and window 2 (W2) in blue shading. The windows are used to quantify the change in cell populations. A vertical dashed line is added at the time-point where cells that were at the inlet port at time zero pass through the imaging field of view, the position of which is determined by the flow velocity of cells in the channel. No data after the dashed line is analysed. Blood settles in the inlet after loading, causing a wave of higher erythocyte density to reach the imaging window. However, as this blood is in the inlet at the start of the experiment, it is always after the cut-off point (dashed line) at which we stop using the data for a channel, and so it does not affect the results. The velocities shown for each channel represent the mean velocity of all the cells tracked within that channel.

in slightly different flow velocities, we grouped the measurements from the channels into low (0-$100\,\mu\mathrm{m\,s^{-1}}$), medium (150-$300\,\mu\mathrm{m\,s^{-1}}$) and high (300-$500\,\mu\mathrm{m\,s^{-1}}$) flow rates. Scatter plots are also shown in Fig. S9. Across the flow velocities tested, there was no significant difference between the lines for any of the flow ranges. There was also no significant difference in the proportion rings at any flow range between the two strains, Fig. 4a. The lack of difference in invasion between 3D7 and NF54 was unexpected, as we had previously characterised the growth rates of these lines, finding that the growth rate of 3D7 was higher than that of NF54, including in shaking conditions that induced fluid motion. In static NF54 has a Parasite Erythrocyte Multiplication Rate (PEMR) 4.2 $\pm$ 0.2, whereas 3D7 has a higher growth rate with a PEMR of 8.7 $\pm$ 0.6, measured in [9].

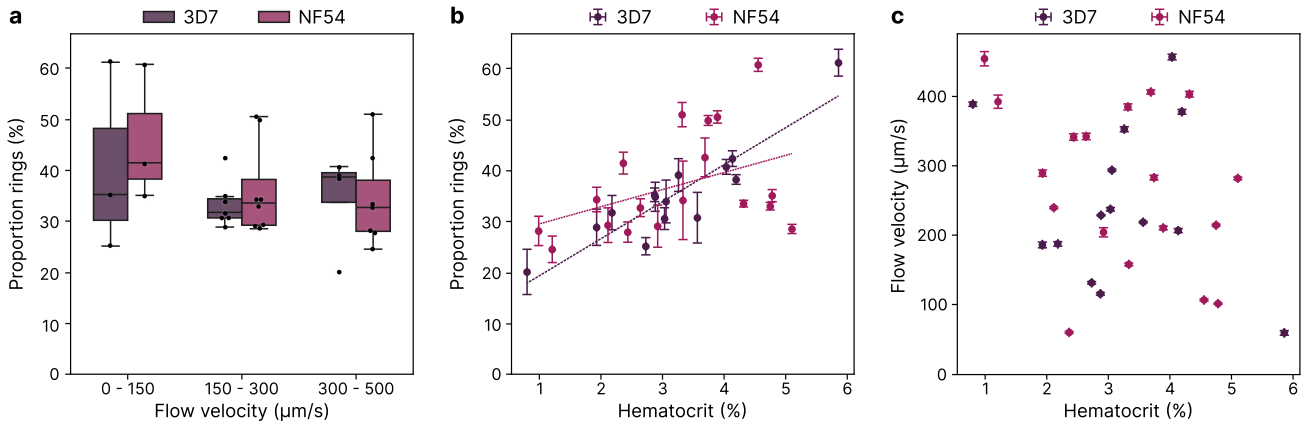

Figure 4: **There is no significant difference in invasion with flow velocity but a positive correlation between invasion rate and haematocrit for wild-type lines NF54 and 3D7.** The data shown is for wild-type lines of NF54 and 3D7. **(a)** Boxplot showing how invasion rate, measured as the proportion of erythrocytes that have invaded to form rings (*proportion rings*), is affected by flow velocity. Flow velocity was binned to low (0-$150\,\mu\mathrm{m\,s^{-1}}$), medium (150-$300\,\mu\mathrm{m\,s^{-1}}$) and high (300-$500\,\mu\mathrm{m\,s^{-1}}$). Each data point represents one channel in one repeat. None of the groups were statistically significant differences as determined by t-tests performed at the 5% significance level ($p < 0.05$). **(b)** A scatterplot of proportion rings vs blood haematocrit is shown. Haematocrit is measured based on the number of erythrocytes observed and the volume of the observed channel. Each data point represents data from one channel and one experiment, with error bars in x and y representing standard deviation. Least squares linear regression is shown with slope m and coefficient of determination $R2$ shown for each strain. **c** The scatterplot of flow velocity vs hematocrit shows how these are independent variables in our experimental setup with no apparent correlation.

2.7 Invasion rate is dependent on haematocrit

Many factor measurements were compared, heamacrit, initial parasitimia, average flow velocity, invasion per schizont, proportion rings and the egress rate, Fig. S9. The most noteworthy relationship was an observed positive correlation between erythrocyte density, measured as haematocrit (HCT), and the invasion rate 4b. Experiments were run with the sample loaded at 10% HCT or 15% HCT, but the resultant haematocrit was measured to be between 1-6% HCT, and even between channels of the same device, the measured HCT varied. We are not sure of the cause of this variation, but it may be due to variability in the efficiency of blood entering the narrow channels possible due to sedimentation of blood at the inlet. For the wild-type lines, the correlation was weaker for NF54 (slope=3.3 and R2 = 0.17) and stronger for 3D7 (slope=7.2 and R2 = 0.82). This correlation is not unexpected because the higher the haematocrit, the greater the probability of a merozoite colliding with an erythrocyte while it is invasion-competent. No correlation was seen between haematocrit and flow velocity 4c, suggesting that such a density of erythrocytes does not impact flow. This scatter also indicates that the relationships presented in 4a are not just a side effect of systematic variations in hematocrit.

2.8 A *P. falciparum* strain lacking the PfEBA175 invasion ligand invades less efficiently under flow conditions

We had previously observed that conditions of high wall shear stress, created by orbital shaking, cause a greater reduction in growth in several genetically modified *P. falciparum* lines in which members of the PfEBA and PfRH invasion ligand family had been individually deleted [9]. Critically, as reported by both us and others, under static conditions these lines grow at the same rate as the wild-type line they are derived from [29, 30, 31, 32, 33, 34, 35]; the invasion defect is only revealed when shear stress is added [9], presumably increasing the forces that oppose merozoites and erythrocytes making productive cell-cell contacts. To explore whether flow conditions could have the same effect, we tested two of these lines using our microfluidic flow approach: ΔPfRH4, in which we had previously seen a weaker effect of shaking on invasion, and ΔPfEBA175, which had the largest reduction in growth under shaking [9]. The invasion efficiency of ΔPfRH4 was not significantly different between low, medium and high flow velocities, just like the wild-type strain from which it was generated, NF54. By contrast, while ΔPfEBA175 invasion was not significantly different to the other lines at a low flow velocity, it was significantly reduced at both medium and high flow velocities, with the proportion of ring-stage parasites reduced more than 2-fold relative to wild-type at the highest flow rate. ΔPfEBA175 also showed a significantly lower invasion rate relative to itself at low flow velocities compared to medium and high flow velocities Fig. 5. This indicates

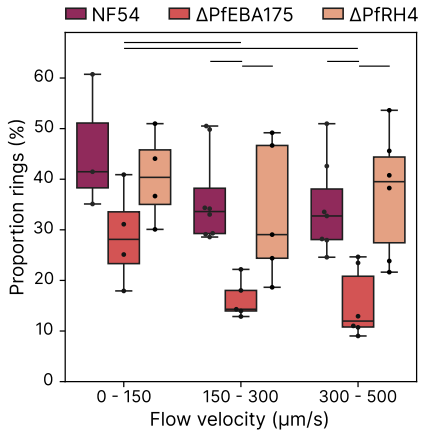

Figure 5: **Increasing flow velocity significantlyreduces the invasion rate of ΔKOPfEBA175.** ΔKOPfEBA175 and ΔKOPfRH4 lines are constructed in the NF54 background. Boxplot showing how invasion rate, measured as the proportion of erythrocytes that have invaded to form rings (*proportion rings*), is affected by flow velocity. Flow velocity was binned to low (0-$150\,\mu\mathrm{m\,s^{-1}}$), medium (150-$300\,\mu\mathrm{m\,s^{-1}}$) and high (300-$500\,\mu\mathrm{m\,s^{-1}}$). The significance lines indicate statistically significant differences between groups, as determined by t-tests performed at the 5% significance level ($p < 0.05$).

that the invasion of lines lacking PfEBA175 is more impacted by flow conditions in the 150-500 um/s range than PfRH4, suggesting that PfEBA175 plays a particularly critical role in merozoite-erythrocyte adhesion under physiological flow conditions. As for the wild-type lines, there is a positive correlation between HCT and invasion rate, Fig. S10a. Again, there was no correlation between haematocrit and flow velocity, Fig. S10b.

3 Discussion

We have developed a novel microfluidic assay in which *P. falciparium* blood stage invasion can occur in a controlled environment where the cells are exposed to shear forces at flow rates comparable to those they experience in the microvasculature. This involved the combination of three elements - design and manufacture of a novel microfluidic setup, careful manipulation and extremely tight synchronisation of the *P. falciparum* parasites and the development of new automated cell identification and tracking software. The result is an assay that can be used to explore invasion in conditions much closer to where invasion occurs *in vivo* for the first time.

Schizonts have been shown to sequester in the microvasculature [5], so the subsequent vasculature is likely a key site of invasion. This device facilitates simultaneous observations at four distinct flow velocities generated through backpressure created by adjustable-height water columns. This allowed us to compare invasion under flow velocities that vary twenty-fold in the same devices ($20\,\mu\mathrm{m\,s^{-1}}$-$450\,\mu\mathrm{m\,s^{-1}}$), Fig. S7. The current limitation to the maximum flow velocity stems from the channel length, as egress and invasion must occur within the microfluidic device for the parasites observed in the imaging region. The time window in which the population exhibits high egress and invasion activity is about 10 minutes for our tightly synchronised samples. The channel in our current devices is $27.7\,\mathrm{cm}$ long, which means the maximum flow velocity we can test is $460\,\mu\mathrm{m\,s^{-1}}$. In the future, improved bonding between the glass and PDMS could enable longer channels, thereby facilitating the testing of higher flow velocities and shear forces. Most of our knowledge about blood flow comes from studies on animals. In humans, measurements from the eye and the finger in post-capillary vessels with diameters of 10-$40\,\mu\mathrm{m}$ have flow velocities of 200-$2000\,\mu\mathrm{m\,s^{-1}}$ and venules that follow with dimensions of 0.1-$20\,\mathrm{mm}$ have flow velocities of 2-$8\,\mathrm{mm\,s}$ [20, 21, 22]. Our channels are $6.7\,\mu\mathrm{m}$ deep and $100\,\mu\mathrm{m}$ wide and had flow velocities of 20-$450\,\mu\mathrm{m\,s^{-1}}$. This means that we are at the lower end of the flow velocities at which invasion is likely to occur *in vivo*, but these measurements are still within the physiological range for the first time, unlike previous video microscopy of invasion under static conditions [36]. It is also important to consider the wall shear stress (WSS) forces to which the cells are exposed in our devices. We are likely achieving a maximum WSS at $450\,\mu\mathrm{m\,s^{-1}}$ of $0.4\,\mathrm{N\,m^{-2}}$, calculated using [37, 38]. This is lower than WSS measured in the human conjunctival capillaries of $1.5\,\mathrm{N\,m^{-2}}$ [21]. We previously saw a significant reduction in growth and invasion rates relative to static in an orbital shaking assay; however, the differences were seen at much higher WSS, with the mean WSS forces simulated to be $2.7\,\mathrm{N\,m^{-2}}$ [9]. Therefore, under conditions of higher WSS, which will hopefully be investigated in the future, the flow velocity is likely to affect growth more significantly than observed in this study.

We have used this device to demonstrate for the first time that invasion of certain *P. falciparum* lines, notably for ΔPfEBA175, is influenced by flow velocity. Over the flow range tested and between wild-type lines, there was no measurable effect on the wild-type lines NF54 and 3D7, Fig. 4a, despite previous assays in static and shaking conditions showing 2-fold differences between these lines when shear forces are increased by shaking on an orbital platform [9]. This suggests that under flow conditions, factors such as contact frequency may dominate other biological factors that drive differences in invasion rates between these lines in static conditions. It is also possible that differences would occur if higher flow rates were tested. The fact that higher flow velocities caused a significant reduction in the growth rate of ΔPfEBA175, however, is in line with previous measurements made under conditions of high WSS generated by growth cultures on a shaking platform. ΔPfEBA175 had the lowest fold-reduction relative to static of all the PfEBA and PfRH knock-out lines tested [9]. This suggests that PfEBA175 is particularly important for merozoite attachment under conditions of high flow and wall shear stress (WSS), such as those found in the microvasculature. The fact that both we and others have previously seen no difference in invasion or growth rates for ΔPfEBA175 under static conditions in the NF54 and 3D7 backgrond [35, 9, 39] emphasises the importance of more nuanced and physiologically relevant assays to explore *P. falciparum* gene function, particularly for highly dynamic processes such as erythrocyte invasion.

This approach could also be applied in the future to investigate other features of the *P. falciparum* invasion process. One such avenue would be a systematic exploration of how different flow velocities impact the invasion of different cell types, such as reticulocytes as compared to the mature erythrocytes used here, erythrocytes from specific blood groups or genetic backgrounds associated with protection from severe malaria, or treated with enzymes like neuraminidase to remove specific invasion receptors. The use of differential fluorescent labelling to distinguish multiple blood types or genetic variants could allow parallel testing in the same device to minimise technical variation, similar to the concept of grouping different blood types together, flow cytometry-based invasion assays [40]. There is also considerable scope for modifying the channel design to investigate the impact of a wide range of different vessel geometries on invasion. The control over the design of the channels using this fabrication approach means that it would also be possible to test different physical perturbations, such as introducing junctions or constrictions. It would be particularly interesting to vary the channel diameters to mimic different vessel dimensions, especially given that this impacts the movement of the blood [41]. Sequestration of schizonts could also be mimicked by introducing pillar-cages into the channel. Late-stage infected erythrocytes are more rigid than uninfected erythrocytes [42, 43], which means that channel restrictions could be set such that erythrocytes, rings and merozoites could pass through, but schizonts could not.

4 Conclusion

We have presented a novel microfluidic device for following malaria parasite invasion under flow for the first time, and used it to show that PfEBA175 may play a critical role in invasion under flow *in vivo*. The system also includes a fully automated cell identification and tracking pipeline, which has the potential to be modified to follow invasion in other scenarios. A further avenue for investigation would be to combine automated invasion quantification with microfluidic devices that closely recapitulate the cellular environment, such as those containing epithelial cells that are currently being used to investigate sequestration [44, 45, 46].

5 Materials and Methods

5.1 Parasite culture

P. falciparum strains (either the wildtype NF54, 3D7 or genetically modified lines ΔPfRH4 or ΔPfEBA175 [29]) were cultured in human erythrocytes purchased from NHS Blood and Transplant, Cambridge, UK under the University of Cambridge Human Biology Research Ethics Committee, HBREC.2019.40 and ethical approval from NHS Cambridge South Research Ethics Committee, 20/EE/0100; the NHS obtained formal written consent for sample collection. The culture was kept at $37\,^{\circ}\mathrm{C}$ in a gassed incubator or gassed sealed culture container under a low oxygen atmosphere of 1% O_2, 3% CO_2, and 96% N_2 (BOC, Guildford, UK). Cultures were routinely maintained at a 4% haematocrit (HCT) in RPMI 1640 media (Gibco, UK) (routine culture was done using RPMI with phenol red and imaging was done without Phenol red which can cause fluorescent background) supplemented with 5 gl^{-1} Albumax II, DEXTROSE ANHYDROUS EP 2 gl^{-1}, HEPES 5.96 gl^{-1}, sodium bicarbonate EP 0.3 gl^{-1} and 0.05 gl^{-1} hypoxanthine dissolved in 2M NaOH.

5.2 Sorbitol synchronisation

Sorbitol synchronisation, described by [47], was performed by pelleting a culture with a large number of ring stage parasites, removing the supernatant and resuspending the pellet in ten times the pellet volume of 5% D-sorbitol (Sigma-

Aldrich). This was incubated at $37\,^{\circ}\mathrm{C}$ for 5 mins, during which time later-stage parasites (trophozoites and schizonts) will rupture. The cells are then pelleted by centrifugation and then resuspended in RPMI at twenty times the pelleted volume. The cells were pelleted again and then resuspended in complete media to give 4% HCT.

5.3 Tight synchronisation of parasitised erythrocytes

After the lines were defrosted, they were sorbitol synchronised in the first cycle when the culture was greater than 0.5% rings and then delayed at room temperature to push the egress window into the intended synchronisation cycle. The parasites are tightly synchronised to a 3-hour window; before beginning, smears were checked to confirm the culture was predominantly schizonts with few rings. The media was removed from the culture, leaving $5\,\mathrm{mL}$ into which the infected blood was resuspended. This is then layered over $5\,\mathrm{mL}$ of 70% Percoll in a $15\,\mathrm{mL}$ tube (Percoll Merck P4937, 10% 10x PBS, 20% RPMI) and centrifuged at 1450 rcf for 11 min with break set to 1 and accelerator to 3. This results in a band of late-stage parasites at the Percoll-media interface, which is removed and added to a flask with media and blood at a 4% HCT and incubated in a gassed incubator at $37\,^{\circ}\mathrm{C}$ for 3 h. The Percoll separation was then repeated as above, but this time, the bottom pellet containing the newly invaded ring stage parasites was kept. Then, sorbitol synchronisation was carried out to remove any remaining late-stage parasites that had not been removed by Percoll separation. This results in parasites that are all within a 3 h developmental window, as they must have invaded new erythrocytes within the 3 h post Percoll-purification. The parasites were then resuspended in $80\,\mathrm{mL}$ culture at 2.5% HCT. Once the parasitemia was higher than 2 % half of the parasites were kept from each cycle to reinvade, and half were used for microfluidics. The parasites for microfluidics were delayed for 28 h at room temperature so that the imaging could be done on a different day from the synchronisation.

5.4 Printing of photoresist on silicon wafer

The mould used to cast the channels was created using soft lithography [48]. The positive of the design was first printed on photoresist film on a silicon wafer. A $11\,\mathrm{mm}$ Silicon Wafer (P(100) 0-100 Ohm-cm 500 μm SSP, University wafer Inc) was first washed with acetone and Isopropanol and then blow-dried with a Nitrogen gun. The wafer was then placed on a hot plate for 10 mins at $200\,^{\circ}\mathrm{C}$ before being left to cool on a lint-free wipe for 90 s at room temperature. The wafer was placed on the chuck of the spin-coated (Laurell Technologies Corporation, model WS-650MZ-23NPP8) and $3\,\mathrm{mL}$ of SU8 6005 (A-Gas) was placed into the centre of the wafer and then spun for $10\,\mathrm{s}$, at 500 rpm acceleration to 100 rpm/s, then for $30\,\mathrm{s}$ at 1900 rpm acceleration to 500 rpm/s. The coating was inspected to ensure an even application, and the process was repeated if any defects were observed. It was then soft-baked on a hot plate at $65\,^{\circ}\mathrm{C}$ for 1 min; then the hot plate was turned up to $110\,^{\circ}\mathrm{C}$ for a further 6 min.

The pattern of the channel was created using a Durham Magneto Optics Microwriter ML 3 to cross-link the photoresist in the area of the channels. A $50\,\mu\mathrm{m}$ resolution was used. Following printing, the wafer was post-exposure baked on a hot plate at $65\,^{\circ}\mathrm{C}$ for 1 min, $95\,^{\circ}\mathrm{C}$ for 6 min, then $65\,^{\circ}\mathrm{C}$ for 1 min. Next, the unexposed photoresist was washed away. It was placed in the SU8 developer (PGMEA (Propylene glycol methyl ether acetate)) for 210 s or until the residue was completely removed and then washed in isopropanol. The wafer was hard-baked on a hot plate at $200\,^{\circ}\mathrm{C}$ for 5 mins. The depth of the channel was then measured using a profilometer (DektaXT, Bruker), resulting in a channel thickness of 6-7 $32\,\mu\mathrm{m}$. The shallow channels ensure a flat layer of erythrocytes, which facilitates their automated tracking.

5.5 Casting Polydimethylsiloxane (PDMS) and assembling devices

The silicon wafer was placed in a square plastic petri dish and visually inspected to check that it was completely free of dust. Polydimethylsiloxane (PDMS) (Sylgard 184 silicone elastomer kit) was made up by vigorously mixing the base with the curing agent (10% of the volume of base). It was degassed in a vacuum chamber and poured over the wafer. The PDMS was then cured at $60\,^{\circ}\mathrm{C}$ for 2 h. As multiple devices are on a single wafer, the individual devices are next cut out with a scalpel with roughly 0.5 cm of PDMS around the channels. The inlet and outlet holes were then punched using a $0.75\,\mathrm{mm}$ hole (Syneo CR0350255N20R4) and a Syneo punch machine. Debris blocking the narrow channels was a major issue, Fig. S3, a large source of this was punching the holes; we found the debris was reduced by cutting holes over a clean piece of PDMS and washing the devices thoroughly after holes were punched. The PDMS devices and glass slides (Adademy glass coverslips, 24 x $32\,\mathrm{mm}$, 0.13-$0.16\,\mathrm{mm}$ thick, 400-03-19) were washed with acetone, isopropanol and then deionised water, then dried using a nitrogen gun and placed channel side up in a petri dish in a $60\,^{\circ}\mathrm{C}$ oven for 10 mins. The PDMS device is then bound to the glass slide using plasma treatment. The clean glass slide and the PDMS device with the channel side up are placed on the tray of the plasma cleaner (Harrick Plasma, Plasma Cleaner PDC-32G and Vacuum Gauge PDC-VCG-2). The chamber was depressurised to 0.1 with the valve down, and then the pressure was set to 0.5 with a valve to the right. The plasma was then activated on high for $30\,\mathrm{s}$. After bonding, the

device was placed for $10\,\mathrm{min}$ on a hotplate set to $90\,^{\circ}\mathrm{C}$ and then left overnight in an oven at $60\,^{\circ}\mathrm{C}$. This step of heating the device after bonding was the factor that most significantly improved our bonding.

5.6 Setup of microfluidics device

Inlet and outlet tubes are connected to the holes in the PDMS devices using PDMS couplers (20G stainless steel $90\,^{\circ}\mathrm{C}$ bent, Darwin Microfluidics PN-BEN-20G-100) and Tygon-tubing (ID $0.020\,\mathrm{in}$ OD $0.060\,\mathrm{in}$, Cole-Palmer ND-100-80). Clamps were added to the two inlet tubes. Loading was done with a luer lock syringe needle (23G blunt-end, Darwin Microfluidics AE-23G-100x). With the pump inlet closed, the channel is blocked by loading 7.5% Bovine Serum Albumin (BSA) in Phosphate-buffered saline (PBS) (Merck A8412) into the loading inlet, and the device was placed at $37\,^{\circ}\mathrm{C}$ for $30\,\mathrm{min}$. Complete Phenol-Red free media was then passed through the channel.

5.7 Microscopy

A field of view close to the end of the channels was imaged at $37\,^{\circ}\mathrm{C}$ using a custom-built, open-frame inverted microscope for 40 minutes. The objective used was a 20x air objective (Plan Apo VC 20x/ 0.75 DIC N2 OFN25 WD 1.0). Videos were recorded with alternate frames in brightfield ($528\,\mathrm{nm}$) and fluorescence ($470\,\mathrm{nm}$) illumination at 100 frames per second, using an LED bandpass fluorescent filter cube. The camera used was a Teledyne FLIR BFS-U3-70S7M-C with a 7.1 MP Sony IMX428 monochrome image sensor, resulting in an effective resolution of $0.224\,\mu\mathrm{m/pixel}$. All images were captured at 3208×1000px, utilising only a portion of the sensor's rows to achieve higher frame rates.

The flow in the channel is driven by a pressure pump (Disc pump evaluation kit P1329 020 XPSZ8 TTP Ventus/The Lee Company). The pressure pump was set to generate $19.2\,\mathrm{kPa}$ at the inlet. The outlet tubes were connected to columns of water of different heights to generate the backpressure that leads to different flow velocities in the channels. The column heights used were 0, 50, 100 and $150\,\mathrm{cm}$, with the highest water column corresponding to $14.7\,\mathrm{kPa}$ added back-pressure and thus the slowest flow velocity. The columns were placed on three-way valves, allowing the removal of the weight of the water columns when loading the microfluidic device with its malaria sample, so that all the channels could be loaded at the same rate.

5.8 Preparation of sample for imaging

The steps for setting up the sample for imaging are summarised in Fig. S4. The tightly synchronised schizonts were arrested prior to egress by first isolating late-stage parasites from the culture using Percoll isolation as described above and then resuspending them in $20\,\mathrm{mL}$ of complete media with $1\,\mu\mathrm{mol}$ Compound 2 [23]. The samples were kept at $37\,^{\circ}\mathrm{C}$ for a minimum of 3 h and a maximum of 5.5 h. As all parasites within the tightly synchronised culture were within a 3 h developmental window, this 3-5.5 h incubation with Compound 2 should arrest the majority of parasites as late schizonts, just before egress. For each round of imaging, $10\,\mathrm{mL}$ of culture was removed from the flask, pelleted by centrifugation, and $9\,\mathrm{mL}$ of media was removed. The pellet was then resuspended in the remaining $1\,\mathrm{mL}$ of the media, ensuring that Compound 2 remained present. Next, Sybr Green (Invitrogen, Paisley, UK) was added to give a 1-in-5000 dilution and then incubation was carried out at $37\,^{\circ}\mathrm{C}$ for $30\,\mathrm{min}$. Two DNA dyes were tested, Sybr Green and Hoechst 33342 and it was shown that the Sybr Green gave a much brighter signal, Fig. S2. Blood was added to give a 10% or 15% HCT, and the parasites were washed twice in $1\,\mathrm{mL}$ of complete Phenol-Red free media to remove Compound 2. Once Compound 2 is removed, merozoites start egressing after roughly $15\,\mathrm{min}$. The culture was loaded into the channel as quickly as possible, with washing and loading usually taking about $10\,\mathrm{min}$. The clamp on the input tubing was then closed, and the clip connected to the pressure pump was opened, with the pump already started. The valves for the outlet tubing were then set so that the water columns were connected to the outlet tubes. The pressure pump was then started, and once it was confirmed that the cells were flowing as expected, the camera recording was started and continued for at least $30\,\mathrm{min}$ to allow for invasion to occur.

5.9 Image analysis

The videos of the cells passing through the microfluidic channels were analysed using automated image analysis to identify the different cell types, and their trajectory across frames was tracked.

Finding erythrocytes The first step is to analyse the brightfield images to detect all erythrocytes. The frames are pre-processed with a Gaussian blur. Then, we find the erythrocytes using the Hough circles implementation in OpenCV, [49] which uses gradient information from edges in the image. The parameters used are: minimum separation $= 12\,\mathrm{px}$, parameter 1 $= 300$, parameter 2 $= 12$, min radius $= 8\,\mathrm{px}$, and max radius $= 30\,\mathrm{px}$. This

approach is effective, as we know the erythrocytes have a round shape, and looking for the contour enables the segmentation of cells that overlap.

Finding schizonts, merozoites, and rings The fluorescent frames are next used to detect the parasites (schizonts, merozoites, and rings) as they are all stained with the SYBR Green DNA dye. This segmentation was performed using edge detection. First, the frames are pre-processed with a Gaussian blur and normalised so each pixel gets values between 0 to 255. A binary threshold determines all pixels with intensity above 28 as foreground, and a second Gaussian blur is applied to filter out spurious pixels and smooth the outline of true fluorescent signals. In order to filter out any background fluorescence, the contours are then detected and filtered to keep only elements with an area greater than $4\,\mathrm{px}$.

Distinguishing schizonts and cell debris from merozoites and rings Schizonts contain 26–32 merozoites within a single erythrocyte[4, 3], resulting in a significantly higher DNA content compared to a single merozoite or ring. Consequently, schizonts produce a much brighter fluorescent signal than merozoites or rings, both in terms of intensity and size.

Cells were classified as merozoites if their intensity per area fell below all defined linear boundaries for the merozoite population. Conversely, cells were categorised as schizonts if their intensity per area exceeded all defined linear boundaries for the schizont population. Any cells that did not satisfy the criteria for either category were classified as debris. The boundaries were manually selected to optimise the separation of rings and schizonts from debris, based on human-labelled datasets, Fig. S5.

Distinguishing merozoites from rings Distinguishing free merozoites from rings is challenging due to their similar fluorescent profiles, making classification based solely on fluorescent images unreliable. To address this, we leveraged the fact that the fluorescent signal of a ring is located within an erythrocyte. However, this approach is complicated by the frequent movement of merozoites near, above, or below erythrocytes within the channels, which can lead to misclassification. To overcome this, we used Trackpy's `NearestVelocityPredict` [50] feature to link segmented masks into cell trajectories. For classification, any erythrocyte and merozoite that remained within their combined radius for the entire duration of their tracked trajectories (and for at least $40\,\mathrm{ms}$) were considered "matched" and reclassified as rings.

5.10 Data availability

All code and raw data supporting the findings of this study are available in the Zenodo repository at `10.5281/zenodo.15399769`.

Acknowledgements

We would like to thank Theresa Feltwell, Nadia Cross and the CIMR and Physics of Medicine Department support staff for their invaluable logistical support; Yen Chun Lin and Margherita Tavasso who worked on previous version of microfluidics devices to follow malaria invasion which were important proofs of concept; Dean Kos and Ishaan Lohia for their assistance and training whilst they were the microfluidics facility managers. This work was funded by Wellcome, grant numbers (220266/Z/20/Z to JR), (222323/Z/21/Z to EK) and (20485/Z/16/Z to VI); EU-EC Marie Curie ITN PyMot (955910 to MK) and Engineering and Physical Sciences Research Council (EPSRC) grant (EP/W004453/1 to PC). For the purpose of open access, the author has applied a CC BY copyright license to any Author Accepted Manuscript Version arising from this submission. The funders played no role in the study design, data collection and analysis, decision to publish, or preparation of the manuscript.

References

[1] WHO. *World malaria report 2022*. WHO, 2022. ISBN 9789240040496. URL `https://www.who.int/teams/global-malaria-programme/reports/world-malaria-report-2021`.

[2] Paul R. Gilson and Brendan S. Crabb. Morphology and kinetics of the three distinct phases of red blood cell invasion by Plasmodium falciparum merozoites. *International Journal for Parasitology*, 39(1):91–96, 2009. ISSN 00207519. doi: 10.1016/j.ijpara.2008.09.007. URL `http://dx.doi.org/10.1016/j.ijpara.2008.09.007`.

[3] Svetlana Glushakova, Amanda Balaban, Philip G. McQueen, Rosane Coutinho, Jeffery L. Miller, Ralph Nossal, Rick M. Fairhurst, and Joshua Zimmerberg. Hemoglobinopathic erythrocytes affect the intraerythrocytic multiplication of Plasmodium falciparum in vitro. *Journal of Infectious Diseases*, 210(7):1100–1109, 2014. ISSN 15376613. doi: 10.1093/infdis/jiu203.

[4] Rachel M. Rudlaff, Stephan Kraemer, Jeffrey Marshman, and Jeffrey D. Dvorin. Three-dimensional ultrastructure of Plasmodium falciparum throughout cytokinesis. *PLoS Pathogens*, 16(6):1–21, 2020. ISSN 15537374. doi: 10.1371/journal.ppat.1008587. URL `http://dx.doi.org/10.1371/journal.ppat.1008587`.

[5] M. Aikawa, M. Iseki, J. W. Barnwell, D. Taylor, M. M. Oo, and R. J. Howard. The pathology of human cerebral malaria. *American Journal of Tropical Medicine and Hygiene*, 43(2 SUPPL.):30–37, 1990. ISSN 00029637. doi: 10.4269/ajtmh.1990.43.30.

[6] Regina Joice, Sandra K Nilsson, Jacqui Montgomery, Selasi Dankwa, Belinda Morahan, Karl B Seydel, Lucia Bertuccini, Pietro Alano, C Kim, Manoj T Duraisingh, Terrie E Taylor, and Danny A Milner. Levels and changes of HDL cholesterol and apolipoprotein A-I in relation to risk of cardiovascular events among statin-treated patients; a meta-analysis. *Circulation*, 6(244):1–16, 2014. ISSN 15378276. doi: 10.1126/scitranslmed.3008882.Plasmodium.

[7] Oranan Prommano, Urai Chaisri, Gareth D.H. Turner, Polrat Wilairatana, David J.P. Ferguson, Parnpen Viriyavejakul, Nicholas J. White, and Emsri Pongponratn. A quantitative ultrastructural study of the liver and the spleen in fatal falciparum malaria. *Southeast Asian Journal of Tropical Medicine and Public Health*, 36(6):1359–1370, 2005. ISSN 26975718.

[8] Britta C. Urban, Tran T. Hien, Nicholas P. Day, Nguyen H. Phu, Rachel Roberts, Emsri Pongponratn, Margret Jones, Nguyen T.H. Mai, Delia Bethell, Gareth D.H. Turner, David Ferguson, Nicholas J. White, and David J. Roberts. Fatal Plasmodium falciparum malaria causes specific patterns of splenic architectural disorganization. *Infection and Immunity*, 73(4):1986–1994, 2005. ISSN 00199567. doi: 10.1128/IAI.73.4.1986-1994.2005.

[9] Emma Kals, Morten Kals, Pietro Cicuta, and Julian C Rayner. Under conditions of high wall shear stress, several PfEBA and PfRH ligands are important for Plasmodium falciparum malaria blood-stage growth, 9 2024. URL `http://biorxiv.org/lookup/doi/10.1101/2024.09.24.614720`.

[10] Rob Driessen, Feihu Zhao, Sandra Hofmann, Carlijn Bouten, Cecilia Sahlgren, and Oscar Stassen. Computational Characterization of the Dish-In-A-Dish, A High Yield Culture Platform for Endothelial Shear Stress Studies on the Orbital Shaker. *Micromachines*, 11(6):552, 5 2020. ISSN 2072-666X. doi: 10.3390/mi11060552. URL `https://www.mdpi.com/2072-666X/11/6/552`.

[11] Bernhard Sebastian and Petra S. Dittrich. Microfluidics to Mimic Blood Flow in Health and Disease. *Annual Review of Fluid Mechanics*, 50(1):483–504, 1 2018. ISSN 0066-4189. doi: 10.1146/annurev-fluid-010816-060246. URL `https://www.annualreviews.org/doi/10.1146/annurev-fluid-010816-060246`.

[12] J. Patrick Shelby, John White, Karthikeyan Ganesan, Pradipsinh K. Rathod, and Daniel T. Chiu. A microfluidic model for single-cell capillary obstruction by Plasmodium falciparum -infected erythrocytes. *Proceedings of the National Academy of Sciences*, 100(25):14618–14622, 12 2003. ISSN 0027-8424. doi: 10.1073/pnas.2433968100. URL `https://pnas.org/doi/full/10.1073/pnas.2433968100`.

[13] Thurston Herricks, Meher Antia, and Pradipsinh K. Rathod. Deformability limits of Plasmodium falciparum-infected red blood cells. *Cellular Microbiology*, 11(9):1340–1353, 2009. ISSN 14625814. doi: 10.1111/j.1462-5822.2009.01334.x.

[14] Quan Guo, Sarah J. Reiling, Petra Rohrbach, and Hongshen Ma. Microfluidic biomechanical assay for red blood cells parasitized by Plasmodium falciparum. *Lab on a Chip*, 12(6):1143–1150, 3 2012. ISSN 14730189. doi: 10.1039/c2lc20857a.

[15] Majid Ebrahimi Warkiani, Andy Kah Ping Tay, Bee Luan Khoo, Xu Xiaofeng, Jongyoon Han, and Chwee Teck Lim. Malaria detection using inertial microfluidics. *Lab on a Chip*, 15(4):1101–1109, 2015. ISSN 14730189. doi: 10.1039/c4lc01058b.

[16] T. M. Geislinger, B. Eggart, S. Braunmüller, L. Schmid, and T. Franke. Separation of blood cells using hydrodynamic lift. *Applied Physics Letters*, 100(18), 2012. ISSN 00036951. doi: 10.1063/1.4709614.

[17] Ying Bena Lim, Juzar Thingna, Jianshu Cao, and Chwee Teck Lim. Single molecule and multiple bond characterization of catch bond associated cytoadhesion in malaria. *Scientific Reports*, 7(1):1–11, 2017. ISSN 20452322. doi: 10.1038/s41598-017-04352-x.

[18] Meher Antia, Thurston Herricks, and Pradipsinh K. Rathod. Microfluidic modeling of cell-cell interactions in malaria pathogenesis. *PLoS Pathogens*, 3(7):0939–0948, 2007. ISSN 15537374. doi: 10.1371/journal.ppat.0030099.

[19] Maria Bernabeu, Celina Gunnarsson, Maria Vishnyakova, Caitlin C. Howard, Ryan J. Nagao, Marion Avril, Terrie E Taylor, Karl B Seydel, Ying Zheng, and Joseph D. Smith. Binding Heterogeneity of Plasmodium falciparum to Engineered 3D Brain Microvessels Is Mediated by EPCR and ICAM-1. *mBio*, 10(3):1–16, 6 2019. ISSN 2161-2129. doi: 10.1128/mBio.00420-19. URL `https://journals.asm.org/doi/10.1128/mBio.00420-19`.

[20] Aristotle G. Koutsiaris, Sophia V. Tachmitzi, and Nick Batis. Wall shear stress quantification in the human conjunctival pre-capillary arterioles in vivo. *Microvascular Research*, 85(1):34–39, 2013. ISSN 00262862. doi: 10.1016/j.mvr.2012.11.003. URL `http://dx.doi.org/10.1016/j.mvr.2012.11.003`.

[21] Aristotle G. Koutsiaris, Sophia V. Tachmitzi, Nick Batis, Maria G. Kotoula, Constantinos H. Karabatsas, Evagelia Tsironi, and Dimitrios Z. Chatzoulis. Volume flow and wall shear stress quantification in the human conjunctival capillaries and post-capillary venules in vivo. *Biorheology*, 44(5-6):375–86, 2007. ISSN 0006-355X. URL `http://www.ncbi.nlm.nih.gov/pubmed/18401076`.

[22] M. Klarhöfer, B. Csapo, Cs Balassy, J. C. Szeles, and E. Moser. High-resolution blood flow velocity measurements in the human finger. *Magnetic Resonance in Medicine*, 45(4):716–719, 2001. ISSN 07403194. doi: 10.1002/mrm.1096.

[23] Margarida Ressurreição, James A. Thomas, Stephanie D. Nofal, Christian Flueck, Robert W. Moon, David A. Baker, and Christiaan van Ooij. Use of a highly specific kinase inhibitor for rapid, simple and precise synchronization of Plasmodium falciparum and Plasmodium knowlesi asexual blood-stage parasites. *PLOS ONE*, 15(7):e0235798, 7 2020. ISSN 1932-6203. doi: 10.1371/journal.pone.0235798. URL `https://dx.plos.org/10.1371/journal.pone.0235798`.

[24] David Walliker, Isabella A. Quakyi, Thomas E. Wellems, Thomas F. McCutchan, Ana Szarfman, William T. London, Lynn M. Corcoran, Thomas R. Burkot, and Richard Carter. Genetic Analysis of the Human Malaria Parasite Plasmodium falciparum. *Science*, 236(4809):1661–1666, 6 1987. ISSN 0036-8075. doi: 10.1126/science.3299700. URL `http://www.sciencemag.org/cgi/doi/10.1126/science.3299700https://www.science.org/doi/10.1126/science.3299700`.

[25] Kara A. Moser, Elliott F. Drábek, Ankit Dwivedi, Emily M. Stucke, Jonathan Crabtree, Antoine Dara, Zalak Shah, Matthew Adams, Tao Li, Priscila T. Rodrigues, Sergey Koren, Adam M. Phillippy, James B. Munro, Amed Ouattara, Benjamin C. Sparklin, Julie C. Dunning Hotopp, Kirsten E. Lyke, Lisa Sadzewicz, Luke J. Tallon, Michele D. Spring, Krisada Jongsakul, Chanthap Lon, David L. Saunders, Marcelo U. Ferreira, Myaing M. Nyunt, Miriam K. Laufer, Mark A. Travassos, Robert W. Sauerwein, Shannon Takala-Harrison, Claire M. Fraser, B. Kim Lee Sim, Stephen L. Hoffman, Christopher V. Plowe, and Joana C. Silva. Strains used in whole organism Plasmodium falciparum vaccine trials differ in genome structure, sequence, and immunogenic potential. *Genome Medicine*, 12(1):6, 12 2020. ISSN 1756-994X. doi: 10.1186/s13073-019-0708-9. URL `https://genomemedicine.biomedcentral.com/articles/10.1186/s13073-019-0708-9`.

[26] Catherine J. Merrick, Rays H. Y. Jiang, Kristen M. Skillman, Upeka Samarakoon, Rachel M. Moore, Ron Dzikowski, Michael T. Ferdig, and Manoj T. Duraisingh. Functional Analysis of Sirtuin Genes in Multiple Plasmodium falciparum Strains. *PLOS ONE*, 10(3):e0118865, 3 2015. ISSN 1932-6203. doi: 10.1371/journal.pone.0118865. URL `https://dx.plos.org/10.1371/journal.pone.0118865`.

[27] Michael J. Delves, Ursula Straschil, Andrea Ruecker, Celia Miguel-Blanco, Sara Marques, Alexandre C. Dufour, Jake Baum, and Robert E. Sinden. Routine in vitro culture of P. Falciparum gametocytes to evaluate novel transmission-blocking interventions. *Nature Protocols*, 11(9):1668–1680, 2016. ISSN 17502799. doi: 10.1038/nprot.2016.096.

[28] Sabine A. Fraschka, Michael Filarsky, Regina Hoo, Igor Niederwieser, Xue Yan Yam, Nicolas M.B. Brancucci, Franziska Mohring, Annals T. Mushunje, Ximei Huang, Peter R. Christensen, Francois Nosten, Zbynek Bozdech, Bruce Russell, Robert W. Moon, Matthias Marti, Peter R. Preiser, Richárd Bártfai, and Till S. Voss. Comparative Heterochromatin Profiling Reveals Conserved and Unique Epigenome Signatures Linked to Adaptation and Development of Malaria Parasites. *Cell Host & Microbe*, 23(3):407–420, 3 2018. ISSN 19313128. doi: 10.1016/j.chom.2018.01.008. URL `https://linkinghub.elsevier.com/retrieve/pii/S193131281830043X`.

[29] Emma Kals, Morten Kals, Rebecca A Lees, Viola Introini, Alison Kemp, Eleanor Silvester, Christine R Collins, Trishant Umrekar, Jurij Kotar, Pietro Cicuta, and Julian C Rayner. Application of optical tweezer technology reveals that PfEBA and PfRH ligands, not PfMSP1, play a central role in Plasmodium falciparum merozoite-erythrocyte attachment. *PLOS Pathogens*, 20(9):e1012041, 9 2024. ISSN 1553-7374. doi: 10.1371/journal.ppat.1012041. URL http://biorxiv.org/content/early/2024/02/13/2024.02.13.580055.abstracthttps://dx.plos.org/10.1371/journal.ppat.1012041.

[30] Wai Hong Tham, Julie Healer, and Alan F. Cowman. Erythrocyte and reticulocyte binding-like proteins of Plasmodium falciparum. *Trends in Parasitology*, 28(1):23–30, 2012. ISSN 14714922. doi: 10.1016/j.pt.2011.10.002. URL http://dx.doi.org/10.1016/j.pt.2011.10.002.

[31] Sash Lopaticki, Alexander G. Maier, Jennifer Thompson, Danny W. Wilson, Wai-Hong Tham, Tony Triglia, Alex Gout, Terence P. Speed, James G. Beeson, Julie Healer, and Alan F. Cowman. Reticulocyte and Erythrocyte Binding-Like Proteins Function Cooperatively in Invasion of Human Erythrocytes by Malaria Parasites. *Infection and Immunity*, 79(3):1107–1117, 3 2011. ISSN 0019-9567. doi: 10.1128/IAI.01021-10. URL https://journals.asm.org/doi/10.1128/IAI.01021-10.

[32] Kristina E.M. Persson, Fiona J. McCallum, Linda Reiling, Nicole A. Lister, Janine Stubbs, Alan F. Cowman, Kevin Marsh, and James G. Beeson. Variation in use of erythrocyte invasion pathways by Plasmodium falciparum mediates evasion of human inhibitory antibodies. *Journal of Clinical Investigation*, 118(1):342–351, 1 2008. ISSN 0021-9738. doi: 10.1172/JCI32138. URL http://content.the-jci.org/articles/view/32138.

[33] Alexander G. Maier, Manoj T. Duraisingh, John C. Reeder, Sheral S. Patel, James W. Kazura, Peter A. Zimmerman, and Alan F. Cowman. Plasmodium falciparum erythrocyte invasion through glycophorin C and selection for Gerbich negativity in human populations. *Nature Medicine*, 9(1):87–92, 2003. ISSN 10788956. doi: 10.1038/nm807.

[34] Tony Triglia, Manoj T. Duraisingh, Robert T. Good, and Alan F. Cowman. Reticulocyte-binding protein homologue 1 is required for sialic acid-dependent invasion into human erythrocytes by Plasmodium falciparum. *Molecular Microbiology*, 55(1):162–174, 1 2005. ISSN 0950-382X. doi: 10.1111/j.1365-2958.2004.04388.x. URL https://onlinelibrary.wiley.com/doi/10.1111/j.1365-2958.2004.04388.x.

[35] Manoj T. Duraisingh, Tony Triglia, Stuart A. Ralph, Julian C. Rayner, John W. Barnwell, Geoffrey I. McFadden, and Alan F. Cowman. Phenotypic variation of Plasmodium falciparum merozoite proteins directs receptor targeting for invasion of human erythrocytes. *The EMBO Journal*, 22(5):1047–1057, 3 2003. ISSN 0261-4189. doi: 10.1093/emboj/cdg096. URL http://emboj.embopress.org/cgi/doi/10.1093/emboj/cdg096.

[36] Greta E. Weiss, Paul R. Gilson, Tana Taechalertpaisarn, Wai-Hong Tham, Nienke W. M. de Jong, Katherine L. Harvey, Freya J. I. Fowkes, Paul N. Barlow, Julian C. Rayner, Gavin J. Wright, Alan F. Cowman, and Brendan S. Crabb. Revealing the Sequence and Resulting Cellular Morphology of Receptor-Ligand Interactions during Plasmodium falciparum Invasion of Erythrocytes. *PLOS Pathogens*, 11(2):e1004670, 2 2015. ISSN 1553-7374. doi: 10.1371/journal.ppat.1004670. URL https://dx.plos.org/10.1371/journal.ppat.1004670.

[37] Fluigent. No Title. URL https://www.fluigent.com/resources-support/support-tools/microfluidic-calculators/shear-stress-calculator/.

[38] Darwin Microfluidics. No Title, 2025. URL https://blog.darwin-microfluidics.com/microfluidic-flow-rate-shear-stress-calculator/.

[39] Emma Kals, Morten Kals, Rebecca A Lees, Viola Introini, Alison Kemp, Eleanor Silvester, Christine R Collins, Trishant Umrekar, Jurij Kotar, Pietro Cicuta, and Julian C Rayner. *Optical tweezers reveal that PfEBA and PfRH ligands, not PfMSP1, play a central role in Plasmodium-falciparum merozoite-erythrocyte attachment*. 2024. ISBN 0000000198271. URL http://biorxiv.org/content/early/2024/02/13/2024.02.13.580055.abstract.

[40] Michel Theron, Richard L. Hesketh, Sathish Subramanian, and Julian C. Rayner. An adaptable two-color flow cytometric assay to quantitate the invasion of erythrocytes by Plasmodium falciparum parasites. *Cytometry Part A*, 77(11):1067–1074, 2010. ISSN 15524922. doi: 10.1002/cyto.a.20972.

[41] Timothy W. Secomb. Blood Flow in the Microcirculation. *Annual Review of Fluid Mechanics*, 49(1):443–461, 1 2017. ISSN 0066-4189. doi: 10.1146/annurev-fluid-010816-060302. URL https://www.annualreviews.org/doi/10.1146/annurev-fluid-010816-060302.

[42] GB B Nash, E O'brien, EC C Gordon-Smith, and JA A Dormandy. Abnormalities in the mechanical properties of red blood cells caused by Plasmodium falciparum. *Blood*, 74(2):855–861, 8 1989. ISSN 0006-4971. doi: 10.1182/blood.V74.2.855.855. URL http://dx.doi.org/10.1182/blood.V74.2.855.855https://ashpublications.org/blood/article/74/2/855/167233/Abnormalities-in-the-mechanical-properties-of-red.

[43] Y. Park, Monica Diez-Silva, Gabriel Popescu, George Lykotrafitis, Wonshik Choi, Michael S. Feld, and Subra Suresh. Refractive index maps and membrane dynamics of human red blood cells parasitized by Plasmodium falciparum. *Proceedings of the National Academy of Sciences*, 105(37):13730–13735, 9 2008. ISSN 0027-8424. doi: 10.1073/pnas.0806100105. URL http://www.pnas.org/cgi/doi/10.1073/pnas.0806100105.

[44] Ying Zheng, Junmei Chen, and José A. López. Flow-driven assembly of VWF fibres and webs in in vitro microvessels. *Nature Communications*, 6, 2015. ISSN 20411723. doi: 10.1038/ncomms8858.

[45] Ying Zheng, Junmei Chen, Michael Craven, Nak Won Choi, Samuel Totorica, Anthony Diaz-Santana, Pouneh Kermani, Barbara Hempstead, Claudia Fischbach-Teschl, José A. López, and Abraham D. Stroock. In vitro microvessels for the study of angiogenesis and thrombosis. *Proceedings of the National Academy of Sciences of the United States of America*, 109(24):9342–9347, 2012. ISSN 00278424. doi: 10.1073/pnas.1201240109.

[46] Christopher Arakawa, Celina Gunnarsson, Caitlin Howard, Maria Bernabeu, Kiet Phong, Eric Yang, Cole A. DeForest, Joseph D. Smith, and Ying Zheng. Biophysical and biomolecular interactions of malaria-infected erythrocytes in engineered human capillaries. *Science Advances*, 6(3), 2020. ISSN 23752548. doi: 10.1126/sciadv.aay7243.

[47] Chris Lambros and Jerome P. Vanderberg. Synchronization of Plasmodium falciparum Erythrocytic Stages in Culture. *The Journal of Parasitology*, 65(3):418, 6 1979. ISSN 00223395. doi: 10.2307/3280287. URL https://www.jstor.org/stable/3280287?origin=crossref.

[48] Xiao-Mei Zhao, Younan Xia, and George M. Whitesides. Soft lithographic methods for nano-fabrication. *Journal of Materials Chemistry*, 7(7):1069–1074, 1997. ISSN 09599428. doi: 10.1039/a700145b. URL https://xlink.rsc.org/?DOI=a700145b.

[49] OpenCV. No Title, 2024. URL https://docs.opencv.org/4.x/da/d53/tutorial_py_houghcircles.html.

[50] Daniel Allan. soft-matter/trackpy: v0.6.4. 2024. doi: 10.5281/zenodo.1213240. URL https://doi.org/10.5281/zenodo.12708864.